**The spectroscopy of hydride in single crystals of $SrTiO_3$ perovskite**

William R. Palfey,*[a] Son-Jong Hwang[b], William A. Goddard III[c], George R. Rossman[a]

Under reducing conditions, $SrTiO_3$ perovskite can exchange up to 20% of its $O^{2-}$ ions for $H^-$ (hydride), greatly influencing its material properties. This not only presents intriguing possibilities for material design, but also for hydrogen sequestration in the deep earth, where perovskite-structured minerals are abundant. However, uncertainties remain surrounding hydride incorporation in $SrTiO_3$, including details of the hydride structural state, and how hydride interacts with the broader defect chemistry of $SrTiO_3$. Additionally, experimental studies of hydride in $SrTiO_3$ and other perovskites may face analytical limitations. The most common methods for characterizing hydride, namely $^1H$ NMR, may not be suitable in all experimental contexts, including materials with relatively low hydride concentrations and *in situ* high-pressure, high-temperature experiments. Here, we present an investigation of hydride in single crystals of $SrTiO_3$ focused on detailed spectroscopic measurements. Through a combination of density functional theory (DFT)-assisted Fourier transform infrared (FTIR) spectroscopy and UV-vis spectroscopy, we observe structural hydride and its effects on the electronic transitions in $SrTiO_3$. These results are compared directly against $^1H$ NMR. We find that, although hydride is sometimes difficult to identify via FTIR, infrared spectroscopy is significantly more sensitive to hydride than $^1H$ NMR. We find that DFT makes accurate predictions about the spectroscopic behavior of hydride in $SrTiO_3$, pointing to the value of *ab initio* techniques in future studies.

*a.* *Division of Geological and Planetary Sciences, California Institute of Technology, Pasadena, CA, USA.*

*b.* *Division of Chemistry and Chemical Engineering, California Institute of Technology, Pasadena, CA, USA.*

*c.* *Materials and Process Simulation Center (MSC), MC 139-74, California Institute of Technology Pasadena, CA, USA.*

## Introduction

The defect chemistry of oxygen-deficient $SrTiO_3$ perovskite is complex and incompletely understood. In particular, the behavior of hydride ions ($H^-$), which are known to occupy oxygen vacancies ($V_O$) in $SrTiO_3$ and other Ti perovskites, has been an active topic of discussion[1–6]. The hydride ion and associated $V_O$ defects can induce interesting material properties, including color changes, transitions to electronic conductivity, and switchable persistent photoconductivity[2,6]. Titanate perovskites in the (Ca,Sr,Ba)$TiO_3$ family have demonstrated an exceptional ability to incorporate high concentrations of hydride, reaching stochiometric "oxyhydride" compositions[1]. These oxyhydride materials not only have their own unique properties, but can also serve as precursors to produce novel mixed anionic materials, like oxynitrides[7]. High hydride compositions are commonly achieved in titanate perovskites through reactions with hydride salts (usually $CaH_2$, among others)[8,9] . For example, the reaction between $SrTiO_3$ and $CaH_2$ can be expressed as:

$$4SrTiO_3 + 3CaH_2 \rightarrow 4SrTiO_2H + Ca(OH)_2 + 2CaO$$

Through this reaction, $O^{2-}$ is replaced directly by $H^-$ and charge balance is achieved by reducing one $Ti^{4+}$ to $Ti^{3+}$:

$$Ti_{Ti}^{\times} + O_O^{\times} \rightarrow Ti_{Ti}^{/} + H_O^{\cdot}$$

This reaction is now well-documented in $CaTiO_3$, $SrTiO_3$ and $BaTiO_3$, with the most extensive characterization carried out via $^1H$ NMR[2–4,6,8]. Through this $Ti^{4+}$ reduction mechanism, up to 20% of all $O^{2-}$ ions may be replaced

by $H^-$ [2]. Although $O^{2-}$-$H^-$ exchange has been firmly established for the titanate family of perovskites, uncertainties remain surrounding the precise nature of the hydride bonding environment, the occupation of the $V_O$ site (either one or two $H^-$ ions could be stable at $V_O$), and the interplay between coexisting $V_O$ and $H^-$ defects. These uncertainties extend to the electronic transitions in hydride- and $V_O$-containing titanate perovskites, where reducing treatments are associated with a wide variety of color and conductivity changes, presumably due to Ti reduction[7,10–12]. Theory has presented multiple scenarios for the distribution of excess charge across reduced Ti ions[4,13], and laboratory studies have yet to clarify the precise origins of the resulting electronic absorptions. Furthermore, only a limited number of techniques have been utilized to directly characterize $H^-$ in titanate perovskites outside of $^1H$ NMR and neutron scattering[1,2,13,14]. Complementary analytical techniques, especially those capable of distinguishing hydrogen speciation, may be necessary to further elucidate hydride's behavior in $SrTiO_3$ and other oxyhydrides.

Fourier transform infrared (FTIR) spectroscopy has demonstrated exceptional utility for observing and characterizing structural hydrogen in oxides. For many scenarios, like in-situ high-pressure experiments, cases of small or limited sample material, low H concentrations, or samples with NMR-incompatible compositions (e.g, high Fe content), infrared represents one of the few viable methods for describing hydrogen speciation. However, with very few exceptions, these measurements have tended to focus on $OH^-$ groups. $OH^-$ is typically easy to observe, with strong infrared-active stretching modes typically occurring in the range of 3600 – 3000 $cm^{-1}$. In contrast, using FTIR to observe hydride is less straightforward. While hydride has been observed via infrared spectroscopy in a handful of instances[15–19], much remains unknown about the infrared behavior of $H^-$. $H^-$ modes are most likely to reside below 1500 $cm^{-1}$ where many other high-intensity modes are typically present, and the locations of these $H^-$ modes are not well known, mainly due to the many possible coordination geometries of $H^-$ and bonded species. Thus, careful predictions about the IR behavior of hydride, via *ab-initio* Quantum Mechanics methods, are key for identifying $H^-$ in FTIR experiments.

The capacity for hydride incorporation in perovskites could also be of interest to the earth science community. Perovskite-structured oxide minerals are the most abundant materials in Earth's mantle and the chemistry and related properties of these materials has direct consequences for planetary-scale processes. Despite the high solubility of $H^-$ in the perovskite structure, hydride has yet to be evaluated in considerations of mantle dynamics and the overall planetary hydrogen budget. Certain perovskite oxyhydrides can be stabilized by elevated pressures[20,21], possibly pointing to favorable $H^-$ incorporation in planetary interiors, but these effects have not been studied extensively. Additionally, the stability of $FeH_x$ phases at lower mantle conditions[22] could provide a potential source of reduced hydrogen for hydride to react with silicate perovskites. Thus, studies of hydride in perovskite phases, including titanate analogues to earth-abundant minerals, represent important steps toward contextualizing the importance of hydride in deep planetary interiors.

We present here the characterization of hydride-doped single crystals of $SrTiO_3$, a material that serves as a test case for characterizing hydride in oxides. Methods for doping single crystals of $SrTiO_3$ with $H^-$ are detailed. Subsequent analyses find that single crystals of $SrTiO_3$ can be doped easily with $H^-$ and the range of temperatures over which this reaction can occur is larger than previously reported for reactions with powdered materials. We also present FTIR and UV-vis spectroscopy of hydride-bearing $SrTiO_3$ samples, documenting the effect hydride has on $SrTiO_3$ color and documenting a hydride-related mode in a perovskite via FTIR for the first time. These results are then compared to density functional theory (DFT) calculations to assess the accuracy of theory for predicting the behavior of $H^-$. The outcomes of this study should have implications for the broader study of hydride in oxides, highlighting the unique role FTIR and DFT can play in analyzing these materials.

## Methods

### Experimental - synthesis

Two different methods were used to prepare $SrTiO_3$ samples for hydride doping via reaction with $CaH_2$. For the first round of synthesis, 2.5 x 2.5 mm wafers of singly polished crystal substrates of $SrTiO_3$ from MSE Supplies® (>99.9% purity, (100) orientation) were pressed into pellets of $CaH_2$ powder to ensure close surface contact and facilitate ion exchange. Sample preparation then took place in an Ar glovebox to further avoid contamination. Crystal slices were immersed in a finely ground $CaH_2$ powder (Thermo Scientific Chemicals, 98% metal basis purity) and pressed into 7 mm diameter pellets using a hydraulic press. A molar excess of $CaH_2$ (~165 mg) was used for each pellet. Two pellets each were placed into 9 mm fused silica tubes, which were then evacuated to 0.01 Pa and sealed using a gas-oxygen torch at a total tube length of ~30 cm.

Sample tubes were placed directly into a tube furnace preheated to the final reaction temperature (600, 700, or 800 °C). All tubes being treated at the same temperature were placed into the furnace at the same time, and two tubes were designated for each treatment time in the sample series (four pellets per temperature-time condition). At the end of a synthesis run, sample tubes were plunged into liquid nitrogen. The crystals were recovered by dissolving the $CaH_2$ pellets in a mixture of isopropyl alcohol and deionized water (~3:1 ratio). The recovered crystals were sonicated in deionized water to remove unwanted reaction products from their surfaces.

Because these pelletized samples were deformed, cracked or shattered either upon recovery or during preparation, a second round of syntheses was carried out to produce samples suitable for transmission spectroscopy (i.e., FTIR and UV-vis). In this round of syntheses, ~3.3 x 10 mm slices of $SrTiO_3$ were packed into a secondary 4 mm ID fused silica tube with $CaH_2$ powder, placed into the bottoms of longer 9 mm tubes and sealed in the same manner as the pelletized samples. The procedure for treatment in the furnace was identical to the pelletized samples, except the tubes were allowed to cool to room temperature in air, rather than being plunged in liquid nitrogen. One sample (SC-70048h) was treated in this manner through two separate 24-hour steps. A more detailed account of the vacuum tube preparation can be found in the SEI.

Samples from the second round of synthesis were thinned and polished in preparation for transmission spectroscopic methods. Due to the high absorptivity of the samples in the infrared range (discussed in more detail in our results), samples needed to be made very thin. For sample SC-6006h, which was less absorbing, this was accomplished through hand polishing using felt pads charged with diamond abrasives (final polish of 0.25 μm). For samples SC-70024h, SC-70036h, and SC-70048h, which needed to be thinned below 20 μm, a dimple grinder (Fischione brand, model M2000, usually used to prepare materials for transmission electron microscopy) was used. Samples were first thinned between 150 and 80 μm, before the dimple grinder was used to bring them to their final thicknesses. During this process, the factory polished side of the crystal was left intact. Final dimpled surfaces were achieved with a 3 μm diamond suspension.

| Sample | Treatment Conditions |
|---|---|
| | |
| **$CaH_2$ Series** | |
| **SC-6006h** | **Reacted with $CaH_2$ for 6 hours at 600 °C** |
| **SC-70024h** | **Reacted with $CaH_2$ for 24 hours at 700 °C** |
| **SC-70036h** | **Reacted with $CaH_2$ for 36 hours at 700 °C** |
| **SC-70048h** | **Reacted with $CaH_2$ in two stages for 24 hours at 700 °C** |
| | |
| **Vacuum Series** | |
| **Vac1** | **Same as SC-70048h, then vacuum annealed 3.5 hours at 500 °C** |
| **Vac2** | **Vac1 vacuum annealed additional 3.5 hours at 500 °C** |
| **Vac3** | **Vac2 vacuum annealed additional 3.5 hours at 600 °C** |
| | |
| **$H_2$ / $D_2$ Series** | |
| **H2-70024h** | **SC-70024h annealed under flowing $H_2$ at 400 °C for 6 hours** |
| **D2-70024h** | **SC-70024h annealed under flowing $D_2$ at 400 °C for 6 hours** |

***Table 1*** *– Overview of the treatment conditions for samples that were measured via transmission spectroscopy.*

Some of the samples treated in the above manner were also subjected to additional treatments for more advanced spectroscopic study. A portion of SC-70048h was vacuum annealed in stages and analyzed between each stage. These consisted of two 500 °C, 3.5 hour steps, and a final 600 °C, 3.5-hour step. A 2 mPa continuous vacuum was pulled on the samples during these treatments. Additionally, two portions of a sample prepared identically to SC-70048h were annealed under $H_2$ and $D_2$ flow, to investigate the H/D exchange. These treatments lasted for 6 hours and were carried out in a tube furnace heated to 400 °C, in a process modeled after prior treatments carried on $BaTiO_3$ powders[2]. Both the vacuum annealed and $H_2/D_2$ annealed samples were polished and dimpled in the manner outlined above.

**Experimental - analytical**

Raman spectroscopy was carried out using a Renishaw inVia Raman microscope equipped with a 514 nm green laser. Static scans were carried out centered at 1100 $cm^{-1}$, for a spectral range of 100 to 2000 $cm^{-1}$. Laser powers ranging from 0.062 to 0.86 mW were used to assess the effect on the sample spectra. Spectra were taken on the manufacturer-polished sides of the samples.

$^1H$ magic angle spinning (MAS) NMR spectra were collected using a Bruker DSX-500 spectrometer and a Bruker 4 mm MAS probe. Samples were diluted with fused quartz powder using a mortar and a pestle and packed into 4 mm zirconia rotor and spun at 12000 Hz. The dilution was performed inside an Ar-filled glovebox in which the humidity is maintained below a few ppm water. This was found to be necessary for samples containing higher concentrations of hydride. A 4 microsecond (μs) 90 degree radiofrequency (rf) pulse at an operating frequency of 500.21 MHz was applied to record free induction decay with a recycle delay time of 10 second. Note that longer delay time (50 s) was tested for ruling out the presence of any slowly relaxing $^1H$ signal. Signal averaging was done for 64 scans unless otherwise noted. The $^1H$ background signal was recorded the same way, and the subtracted signal is reported. The $^1H$ chemical shift was externally calibrated to tetramethylsilane (TMS) while Tetrakis-(trimethylsilyl)silane (TKTMS) was used as the second reference.

Infrared spectroscopy was carried out using a Thermo-Nicolet iS50 FTIR spectrometer equipped with a KBr beamsplitter and MCT-A liquid nitrogen cooled detector. Attenuated total reflectance (ATR) was found to be insufficient for these materials (either due to high sample absorptivity, high refractive indices, low H concentrations or a combination of the three), so transmission spectroscopy was used instead. Both white and IR light sources were used to probe an extended range (7500 to 2500 $cm^{-1}$ and 5500 to 650 $cm^{-1}$ for each source, respectively). For highly absorbing samples, the maximum number of accumulations allowed by the instrument per measurement was reached (60000 scans). Liquid nitrogen temperature spectra (which would normally be preferable for resolving peaks) could not be collected, as the windows of our low-temperature apparatus increased reflection loss, frequently truncating features in the critically important high-absorbance, low frequency spectral range.

Optical absorbance spectra covering the visible and near infrared range were collected on a custom made 1024 element silicon diode array spectrometer with a tungsten-halogen light source. By using switching between two different detectors, spectra over the range of 380 to 1700 nm (about 26300 to 5900 $cm^{-1}$) could be collected. These results were combined with the FTIR spectra, to produce continuous spectra with an extended range.

**Theory**

DFT calculations were used to predict the likely structural states of hydrogen in $SrTiO_3$ and to predict their infrared characteristics. All calculations were all carried out using the Vienna Ab Initio Simulation Package (VASP, ver 6.2.1 16May21). The Perdew-Burke-Ernerhof (PBE) generalized gradient approximation functional was utilized to describe the exchange correlation, while the D3 corrections of Grimme et al[23–28] was used to describe the van der Waals interactions For total energies, smearing near the Fermi level was done through the tetrahedron method with Blöchl corrections[29] while the cutoff energy for the planewave basis set was fixed to 500 eV. Structural minimizations were converged to an interatomic force of 0.1 eV/Å. Due to the likelihood of unpaired valence electrons resulting from $Ti^{3+}$ states, spin polarized calculations were conducted for all systems described below. The unit cell parameters for all calculations were fixed to the commonly observed experimental value of *a*=3.905 Å at 298K. Supercell sizes of 2×2×2, 3×2×2, 3×3×2 and 3×3×3 were tested. The k-points were generated using an automatically generated Γ-centered grid and optimal k-point densities were converged for each supercell size.

For all supercell sizes, only a single O site was considered for $H^-$ occupation. Given the supercell sizes tested, the effective compositions tested were $Sr_8Ti_8O_{23}H_1$, $Sr_{12}Ti_{12}O_{35}H_1$, $Sr_{18}Ti_{18}O_{53}H_1$, and $Sr_{27}Ti_{27}O_{80}H_1$, effectively spanning a plausible range of hydride concentrations. Multiple positions and configurations of $H^-$ were considered due to the possibility of off-site occupation (a possibility raised by Misaki et al. (2019) in the $BaTiO_3$ perovskite system[3]). Multiple $H^-$ positions were considered, including instances where $H^-$ resides directly at the $O^{2-}$ lattice site, and offsite occupations biased in the direction of two Sr atoms, biased toward one Ti site along the Ti-H-Ti bonds, and biased toward two Sr atoms and one Ti atom (seen in supplementary figure S.1).

The infrared behavior of hydride was predicted through two methods: density functional perturbation theory (DFPT) for the minimized structure (referred to as 0 K) and analysis of trajectories from quantum mechanics molecular dynamics (QM-MD) simulations at various temperatures. DFPT calculations were carried out so that the Born effective charges were calculated simultaneously, which in conjunction with the Hessian produced from DFPT, allows prediction of infrared activities (a code developed by David Karhanek was used to accomplish this in post-processing[30]). Due to practical limitations of computational cost, the largest supercell for DFPT was 3×2×2.

The QM-MD simulation was carried out using a canonical (NVT) ensemble at 300 K (near the temperature of our experiments) using a Nose-Hoover thermostat. The total simulation time was 20 ps, with 1 fs timesteps (20,000 frames). Due to limitations of computational cost, QM-MD simulations were carried out on a 2×2×2 supercell and a single Γ-centered k-point. It was necessary to fix the smearing width at 0.1 eV to allow for reasonably fast electronic convergence at each simulation step. The vibrational density of states was produced from the trajectories by taking the Fourier transform of the velocity autocorrelation function (VACF), as implemented in the 2PT code[31–33].

## Results and discussion

### DFT calculations

The calculations revealed that the bonding geometry of the hydride ion is simple with few structural possibilities. Tests of various occupations of the oxygen vacancy site by hydride predicted that multiple hydride bonding environments are only stable in the smallest supercell (2×2×2). Of the four cases tested, only two were stable in the 2×2×2 cell:

- The onsite direct occupation of the O lattice site by hydride, leading to a Ti-H-Ti bond angle of 180°, and
- An offsite occupation in which H moves toward two of the four adjacent Sr atoms, leading to a Ti-H-Ti angle of 169°. This is the “Sr-biased” structure in supplementary figure S.1.

The offsite occupation is favored by 25 meV for the smallest cell, suggesting that it is the dominant defect state. However, for all supercells 3×2×2 or larger, only the on-site occupation by $H^-$ was found to be stable. These results suggest that the bonding environment of H could differ depending on its concentration. Nevertheless, as is discussed in more detail below, the concentration regime for $H^-$ in samples is not likely to reach the threshold necessary for this multisite occupation via the synthesis method employed here. Thus, mainly the on-site occupation was considered.

The 0 K phonon calculations (which include both DFPT and finite differences) predict three vibrational modes for the $H^-$ ion: a Ti-H-Ti stretching mode centered approximately at 1300 $cm^{-1}$, and two degenerate bending modes located close to 820 $cm^{-1}$. From the DFPT results, the stretching mode is predicted to be strongly infrared active, while the bending modes should only be weakly infrared active. The vibrational density of states produced from the MD simulation carried out at 300 K shows a distribution of modes largely consistent with the DFPT mode positions. Isolation of the H-dominant vibrational density shows a distribution of modes between 1200 and 1400 $cm^{-1}$, with the highest density peak centered at ~1282 $cm^{-1}$. This high-density portion of the distribution implies a prominent line shape for the Ti-H-Ti stretching mode, which should make infrared detection possible.

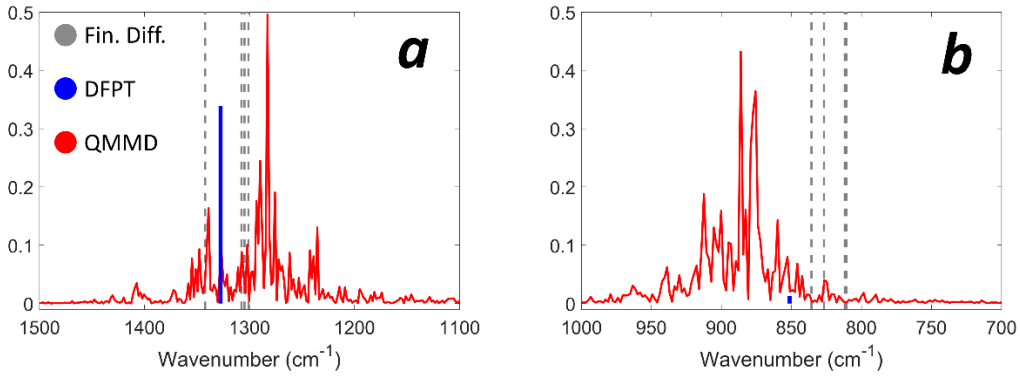


***Figure 1*** *– Summary of the predicted vibrational modes associated with H- in hydride via finite differences, DFPT (0K) and QM-MD (300K) , across a range of supercell sizes. In all cases, the Ti-H-Ti stretching mode (a) is the feature most likely to be detected. It should be positioned approximately in the vicinity of 1300 cm-1. The Ti-H-Ti bending mode (b), is predicted to be significantly weaker and located in a much more absorbing spectral region.*

These DFT results imply specific difficulties for $H^-$ detection via FTIR. First, the predicted position of the Ti-H-Ti stretch overlaps with a native feature of the $SrTiO_3$ spectrum centered at 1326 $cm^{-1}$. Depending on the true position of the stretching mode, hydride's presence may only be apparent upon performing spectral subtractions to remove the 1326 $cm^{-1}$ mode. An additional and more challenging obstacle to overcome is the high infrared absorbance of reduced $SrTiO_3$. As prior authors have noted, spectra of O-deficient $SrTiO_3$ crystals tend to contain a broad, intense feature centered in the infrared (~2200 $cm^{-1}$)[12,34]. The shape of this feature implies an electronic absorption origin. Because of the extreme breadth of this electronic feature, regions below 2200 $cm^{-1}$, including the region likely to contain the Ti-H-Ti stretch, may be inaccessible for measurement. Earlier studies have remarked on this analytical challenge as a barrier to $H^-$ detection via FTIR[5]. These factors also make detection of the bending hydride modes even less likely, as they are in a region of still higher absorbance and have a lower predicted infrared activity. For this reason, only the stretching mode was focused on during experiments.

**Experimental – the pellet samples**

The samples prepared via the pressed pellet method served as the baseline for assessing the $^1H$ NMR behavior of hydride in single crystal $SrTiO_3$. For all treatment conditions, the resulting crystals were extremely dark blue,

becoming more intensely colored with increased temperatures and reaction times. These types of color changes are commonly associated with $H^-$ incorporation in $BaTiO_3$ [2] and have been described for reduced $SrTiO_3$ [10]. Our $^1H$ NMR results for the 800 °C series are presented in Figure 2. For all treatment times in the 600 °C and 700 °C series (which are presented in supplementary figure S.2), $^1H$ NMR does not convincingly detect any features that can be attributed to structural incorporation of $H^-$. Despite this, the clear presence of structural $H^-$ was observed in the samples heated at 800 °C for all three treatment times. The positions and shapes of these features, which are broad with spinning sidebands and negatively shifted, are consistent with $H^-$ signals reported for other titanate perovskites[2–4,9]. Additionally, these features shift to increasingly negative positions with increased treatment time, which is consistent with increased $H^-$ (and possibly $v_O$) content[3,4].

These results could suggest that treatment conditions of 600 °C to 700 °C are incapable of introducing $H^-$ into $SrTiO_3$, perhaps representing a limitation to treatment temperatures as was observed by Guo et al. (2020) with LiH treatments of $BaTiO_3$ [9]. However, this is likely not the case. The clear presence of structural $H^-$ in the 800 °C treated samples rules out an upper limit to $H^-$ incorporation. Therefore, the apparent lack of $H^-$ features is more likely a manifestation of the significantly slower H-O exchange kinetics in single crystals as compared to powder samples. This still leaves open the possibility for $H^-$ in our 600 °C and 700 °C treated samples, albeit at concentrations too low to detect via $^1H$ NMR when the measurement is conducted without a hyperpolarization method[35]. Although $^1H$ NMR detection with hyperpolarization was not pursued in this work, the potential of deeper understanding of these materials by NMR is expected to be high as the field is growing fast.

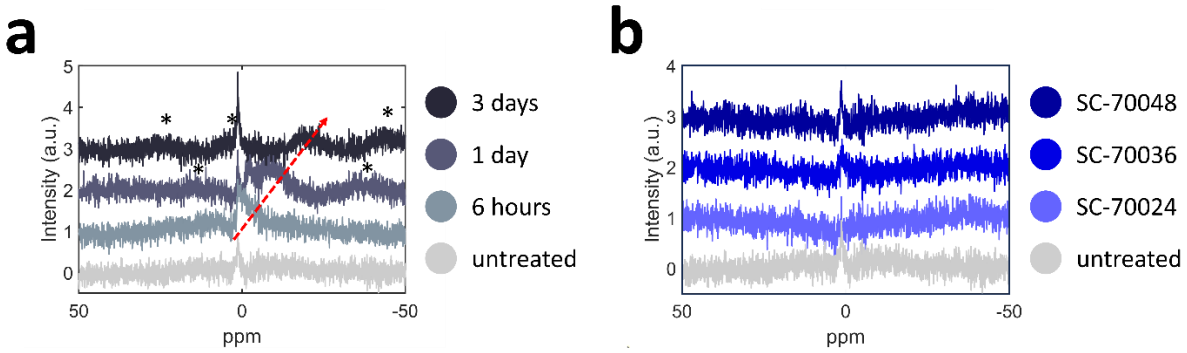


***Figure 2*** *– $^1H$ NMR results for the pelletized samples treated at 800 °C (**a**) and the capsule-method samples that were measured via FTIR and UV-vis spectroscopy (**b**). In the case of the pelletized samples, hydride incorporation has clearly taken place, as evidenced by the emergence of a broad, negative shifted peak that shift progressively more negative (indicated by red arrow). For the capsule-method samples, there is no such feature detectable, only a signal from surface $OH^-$ contamination around 1 ppm. Spinning sidebands of $^1H$ MAS NMR signal are marked with *.*

**Experimental – the capsule samples**

Just like the pressed pellet samples, the capsule-prepared samples did not show detectable structural H via $^1H$ NMR (see Figure 2). Also like the pressed pellet samples, the capsule samples turned a deep blue color, appearing completely opaque in the case of the most intensely treated samples (Figure 3). Because the $CaH_2$ treated samples were so strongly absorbing, they had to be made exceptionally thin to observe the predicted Ti-H-Ti modes near 1300 $cm^{-1}$. In the most extreme case, acceptable transmission through sample SC-70048h was achieved after grinding it to a thickness of ~2.5 µm. A series of combined IR and visible light transmission spectra from 650 to 26500 $cm^{-1}$ for the suite of capsule samples are presented in Figure 3. A summary of the key spectral features discussed here and in later sections is presented in Table 2.

| Feature position | Physical origin | Assignment |
|---|---|---|
| 1308 $cm^{-1}$ | Vibrational mode | Ti-H-Ti stretch |
| 1326 $cm^{-1}$ | Vibrational mode | Native to $SrTiO_3$ |
| 2170 $cm^{-1}$ | Electronic - IVCT | $Ti^{3+}$-$Ti^{4+}$ IVCT via $O^{2-}$ ligand |
| 585 nm | Electronic – IVCT | $Ti^{3+}$-$Ti^{4+}$ IVCT via $H^-$ ligand |
| 513 nm | Electronic – d-d transition | $Ti^{3+}$ d-d transition |

***Table 2*** *– Summary of the spectral features observed and described in this work.*

Consistent with prior studies, reduction of SrTiO3 produces a broad band centered in the infrared region, at approximately 2170 $cm^{-1}$ [11]. This feature has been previously documented when $SrTiO_3$ is reduced under a variety of conditions and is likely related to the reduction of $Ti^{4+}$ to $Ti^{3+}$ and production of oxygen vacancies[11,12]. Its full width half maximum in our samples is ~3000 $cm^{-1}$, consistent with an intervalence charge transfer (IVCT) process (note that this feature's location makes it difficult to isolate to accurately measure the width). In this case, IVCT likely occurs between adjacent O-bonded Ti sites, where delocalized excess charge is transferred between Ti, resulting in transitions between ephemeral $Ti^{3+}$ and $Ti^{4+}$ states. In the present measurements, the intensity of this feature increases in conjunction with increased treatment times and temperatures, consistent with progressive oxygen loss. As expected, this electronic feature makes transmission in the further reaches of the infrared difficult to achieve.

In addition to the 2170 $cm^{-1}$ band, an absorption centered at 585 nm emerges that is responsible for the deep blue color. The full width half maximum value of the absorption is approximately 3200 $cm^{-1}$, consistent with $Ti^{4+}$-$Ti^{3+}$ IVCT seen in hibonite, for example[36]. In prior work done on $BaTiO_3$ powders, a transition to a blue color is closely associated with hydride incorporation[2], and this could also be the case for these $SrTiO_3$ samples. Although there have been previous mentions of a dark violet-blue color in reduced $SrTiO_3$, these studies do not make specific claims about the possible role of hydrogen in contributing to color changes[10]. Regardless, the causes of this 585 nm IVCT band are clearly distinct from the 2170 $cm^{-1}$ band, as the latter can be induced through reduction under vacuum, in the complete absence of hydrogen[11]. The difference between these two absorptions can be explained by considering how bonded ligands can affect IVCT. In $SrTiO_3$ with oxygen vacancies alone, delocalized electrons travel across $O^{2-}$ as the ligand bridging adjacent Ti sites. This results in the 2170 $cm^{-1}$ band. When $H^-$ is the ligand species, the energy of this electron transfer should differ from $O^{2-}$, which is the probable origin of the 585 nm absorption. Hydride-containing $SrTiO_3$ contains both $H^-$ and $O^{2-}$, so both features will be present in hydride-bearing samples. Correspondingly, the presence of other anions would likely result in other electronic features, as is the case of nitride-doped BaTiO3, which is green in color[7].

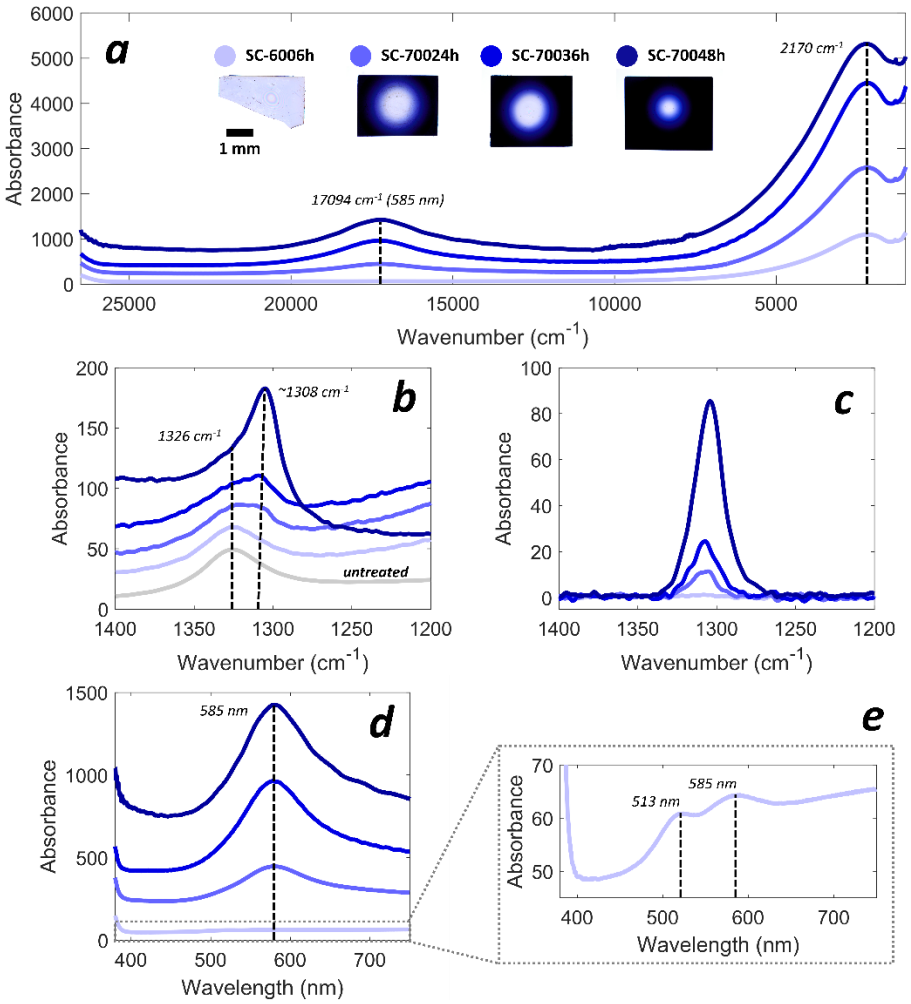


***Figure 3 –*** *The transmission spectra collected from the $CaH_2$ capsule series of samples. All spectra have been normalized to a pathlength of 1 cm.* ***(a)*** *The extended range compilation of visible and infrared spectra showing the relative intensities of electronic and vibrational features. Transmitted light sample images are also show the decrease in transparency with more extended treatments. The 2170 $cm^{-1}$ IVCT feature is dominant.* ***(b)*** *The 1300 $cm^{-1}$ region, showing both the emergent 1308 $cm^{-1}$ mode superimposed on the native 1326 $cm^{-1}$ feature* ***(c)*** *The isolated 1308 $cm^{-1}$ feature.* ***(d)*** *The visible light region presented in units of wavelength, emphasizing the H-associated 585 nm feature responsible for the blue sample color.* ***(e)*** *A zoomed-in view of the SC-6006h spectrum shows the coexistence of two absorptions, whereas all other spectra appear to only contain the 585 nm band.*

FTIR spectra of $SrTiO_3$ subjected to the $CaH_2$ treatment contain a vibrational mode that is superimposed on 1326 $cm^{-1}$ feature, ranging from 1308 $cm^{-1}$ to 1305 $cm^{-1}$ (Figure 3). For simplicity, this will be referred to this as the 1308 $cm^{-1}$ feature. Longer sample treatment times cause the strength of this 1308 $cm^{-1}$ feature to increase in intensity, eventually becoming dominant over the native mode at 1326 $cm^{-1}$. Given the 1308 $cm^{-1}$ feature's correlation with $CaH_2$ treatment, and that its position is consistent with the finite difference, DFPT, and QMMD calculations, we assign this mode as the Ti-H-Ti vibrational mode. However, it should be noted that the lack of corresponding $^1H$ NMR features that correlate directly with the 1308 $cm^{-1}$ feature makes this assignment somewhat tenuous. Indeed, the intensity of the 1308 $cm^{-1}$ band also seems to approximately correlate to the 2170 $cm^{-1}$ IVCT band, meaning that it could possibly be the result of an oxygen vacancy related structural distortion, rather than a hydride mode. Thus, further testing in the form of vacuum annealing and H/D exchanges were necessary to assign the 1308 $cm^{-1}$ mode to hydride.

**Vacuum Annealing**

The progressive vacuum annealing of SC-70048h resulted in dramatic visual and spectroscopic changes. Like all the $CaH_2$ treated crystals, SC-70048h was initially an extremely dark blue color, only achieving transparency when made extremely thin. However, after vacuum annealing, it became significantly more transparent and light purple in color (Figure 4). Subsequent vacuum annealing further reduced this purple color until the sample was completely colorless. Correspondingly, both the FTIR and visible light spectra of Vac1, Vac2, and Vac3 show these changes through the disappearance of the 585 nm IVCT band, the extreme reduction and eventual elimination of the 2170 $cm^{-1}$ IVCT band, and the appearance of a new visible light absorption centered at 513 nm (Figure 4). After appearing in the initial vacuum annealed spectrum, this feature also was eliminated with additional vacuum heating. The full width half maximum of the 513 nm band is 1940 $cm^{-1}$, making its position and shape more consistent with a *d-d* transition from an isolated $Ti^{3+}$ site[37], rather than . The intensity of this band is also consistent with a *d-d* transition, as it is significantly weaker than its 585 nm IVCT counterpart. For a Ti-based oxide, isolated $Ti^{3+}$ centers associated with a localized excess charge are unusual, as the reduction of $Ti^{4+}$ almost universally leads to IVCT.

Vacuum annealing also led to the reduction and eventual elimination of the 1308 $cm^{-1}$ feature. As its intensity was reduced, this feature shifted to slightly higher wavenumbers. Interestingly, there is an apparent decoupling between the 1308 $cm^{-1}$ and 585 nm bands, which seemed to be strongly correlated in the $CaH_2$ series of experiments. However, because both the 585 nm and 513 nm absorptions correspond to $Ti^{3+}$, just with different charge localization, there still seems to be a link between the 1308 $cm^{-1}$ feature and $Ti^{3+}$. Unfortunately, because the reduction of the 1308 $cm^{-1}$ feature also corresponded to the reduction of all other features associated with $SrTiO_3$ reduction (especially the 2170 $cm^{-1}$ band), the vacuum heating analysis did not conclusively distinguish the origin of the 1308 $cm^{-1}$ mode as resulting from either hydrogen incorporation or structural distortion due to oxygen vacancies. As a consequence, deuteration experiments became necessary to make a confident assignment of the 1308 $cm^{-1}$ mode.

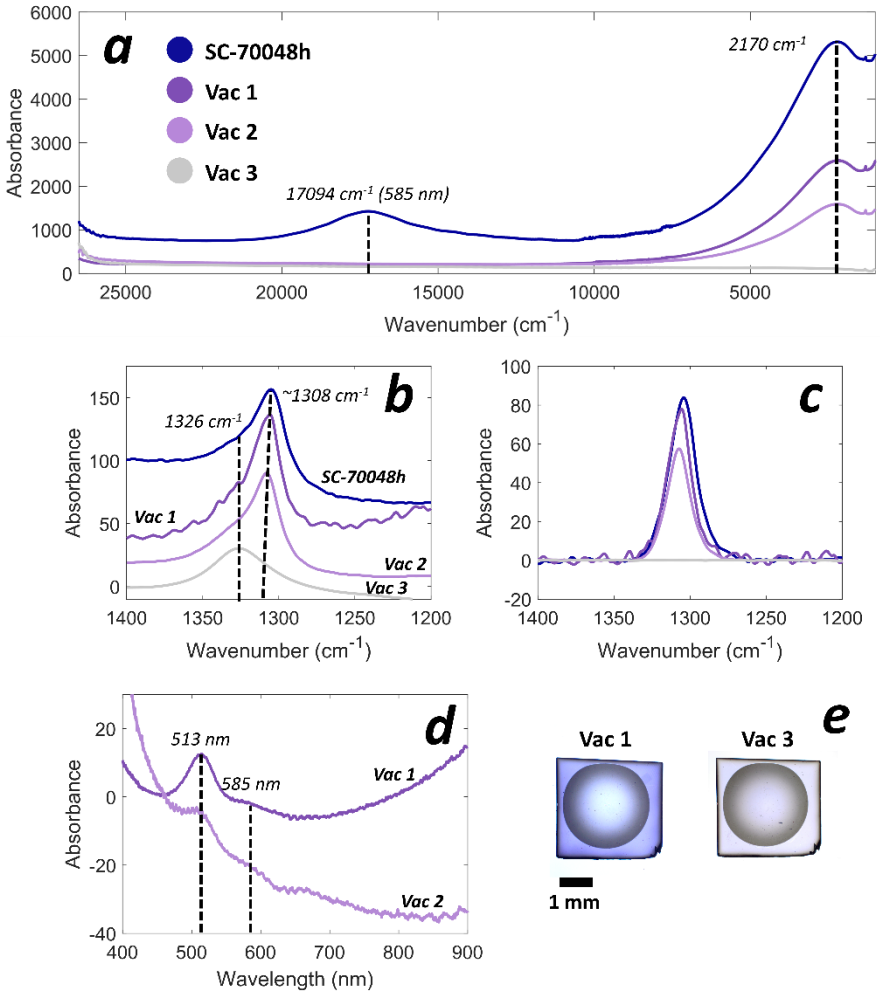


***Figure 4*** *– The transmission spectra collected from the vacuum annealed samples, presented in comparison to their parent material, SC-70048h. All spectra have been normalized to a pathlength of 1 cm.* ***(a)*** *Extended range compilation of visible and infrared spectra. The dramatic difference in intensity between the 513 nm and 585 nm features can be seen in this view and the progressive decrease in intensity of the 2170 cm$^{-1}$ IVCT band is also apparent.* ***(b)*** *The 1300 cm$^{-1}$ region, showing the 1308 cm$^{-1}$ mode superimposed on the native 1326 cm$^{-1}$ feature.* ***(c)*** *The isolated 1308 cm$^{-1}$ feature, which gradually diminishes before completely disappearing.* ***(d)*** *A zoomed-in view of the 513 nm bands in Vac1 and Vac2. A small portion of the 585 nm IVCT band remains in the Vac1 spectrum.* ***(e)*** *Transmitted light images of Vac1 and Vac3, highlighting the dramatic color changes from SC-70048h.*

### H-D Exchange experiments

The starting material for the deuterium exchange was a crystal reacted with $CaH_2$ at 700 °C for 24 hours, equivalent to sample SC-70024h. A single sample was sliced for multiple treatments. Because prior experiments on $SrTiO_3$ have indicated that $H_2$ annealing may cause changes in color for reduced samples, indicating altered defect chemistry[34], the effects of both $H_2$ and $D_2$ annealing were tested. Much like with the vacuum annealed samples, both the $H_2$ and $D_2$ annealed samples underwent a dramatic color change, going from nearly opaque and dark blue to more transparent and a grayish purple color. This color change also corresponded to a virtual elimination of the 585 nm IVCT band and the emergence of the narrower 513 nm *d-d* band (Figure 5), resulting in nearly identical visual absorptions for both samples. Additionally, the 2170 cm$^{-1}$ IVCT band remained very similar in intensity between the two samples, albeit significantly diminished when compared to samples subjected only to the $CaH_2$ treatment.

The only spectral feature that differed significantly between H2-70024h and D2-70024h was the 1308 cm$^{-1}$ band, which somewhat diminished in the $D_2$ sample compared to the $H_2$ sample. Ideally, the emergence of a

corresponding Ti-D-Ti mode located at ~920 $cm^{-1}$ would serve as an indicator for deuterium incorporation, but this was not possible to observe in sample D2-70024h. Thus, a reduction of the 1308 $cm^{-1}$ served as a proxy for deuteration. Initially, the degree to which the 1308 $cm^{-1}$ band was reduced in the $D_2$ annealed sample appeared to be rather minor, with integrated intensities diminished by about 20 – 30%. However, it was determined that the lowering of the 1308 $cm^{-1}$ feature was more pronounced closer to the pristine, factory-polished surface that was directly exposed to the $D_2$ gas flow. This analysis was accomplished by grinding a dimple into the center of each sample, effectively producing a concave wafer of variable thickness. By measuring spectra in sections with different thicknesses (i.e, different spots within the dimple), and normalizing these spectra to sample thickness, it was found that the normalized intensity of the 1308 $cm^{-1}$ feature in the $D_2$ annealed sample changed in response to path length (Figure 6). More specifically, analyses in thinner sections of the deuterated sample corresponded to a greater proportional reduction of the 1308 $cm^{-1}$ band. This was not observed in the $H_2$ annealed sample, which had essentially unchanged normalized intensities regardless of path length. Ultimately, sample volumes closer to the surface of the crystal saw a 90% or greater reduction of the 1308 $cm^{-1}$ feature's intensity when comparing $D_2$ to $H_2$ treatments. This implies a gradient for the integrated intensity of the 1308 $cm^{-1}$ band relative to the sample surface in the $D_2$ annealed sample, suggesting successful H/D exchange. Thus, the 1308 $cm^{-1}$ feature can confidently be assigned to hydrogen. Furthermore, this mode position is highly consistent with the DFT results, so this band is assigned to the Ti-H-Ti stretching mode.

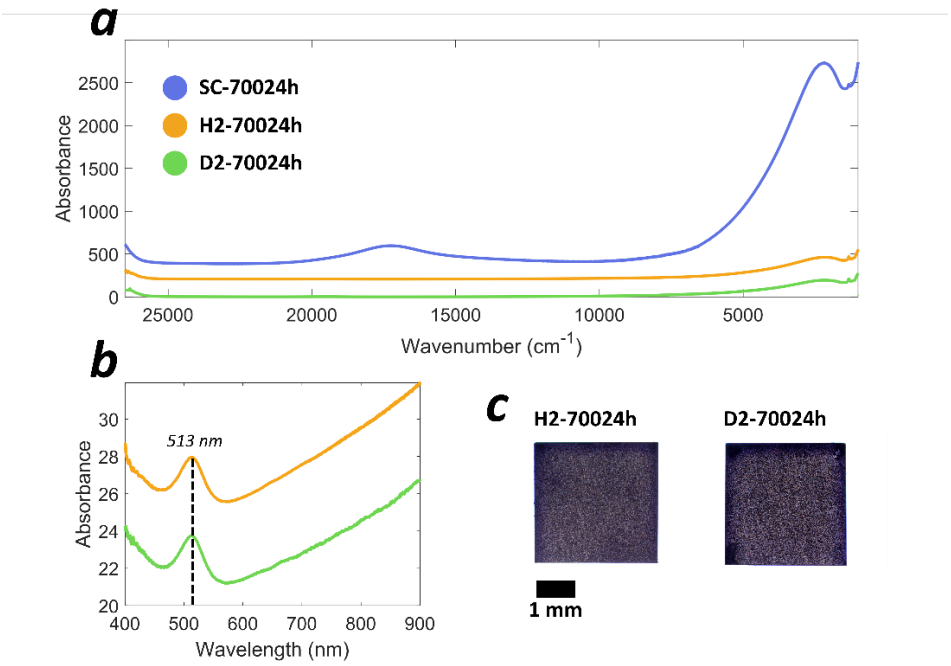


***Figure 5*** *– The transmission spectra collected from the hydrogen and deuterium annealed samples, presented in comparison to SC-70024h. All spectra have been normalized to a pathlength of 1 cm.* ***(a)*** *Extended range compilation of visible and infrared spectra. The decrease in the 2170 $cm^{-1}$ IVCT band compared to SC-70024h is significant.* ***(b)*** *Zoomed in view of the visible light region for H2-70024h and D2-70024h showing approximately equivalent intensity 513 nm bands.* ***(c)*** *Transmitted light view of the two samples at full 500 µm thickness. They have both turned a purple-gray color and are noticeably darker near their edges.*

As previously mentioned, direct observation of a deuterium-shifted mode in proximity to ~920 $cm^{-1}$ would have been great to verify a shift due to hydrogen-deuterium exchange. However, while we were able to observe transmission in this region for thinner portions of sample D2-70024h, there are not obvious features near 920 $cm^{-1}$ that can be attributed to Ti-D-Ti stretching (see supplementary figure S.4). This may be because this

spectral region is heavily influenced by the intense absorptions present below ~800 $cm^{-1}$, which produce steeply sloping spectra with intensities that vary nonlinearly with artificially truncated features. Additionally, if the deuterium mode is just a few 10s of $cm^{-1}$ lower than predicted (920 $cm^{-1}$), it would be further into this problematic low wavenumber region. Nevertheless, the significant decrease in the 1308 $cm^{-1}$ feature for the $D_2$-annealed samples strongly suggests that the 1308 $cm^{-1}$ feature is the hydrogen-associated mode. This is underlined by the fact that all other spectral features between the two samples are nearly identical, suggesting that their defect chemistries are otherwise the same, and by the general consistency between the DFT results and the position of the 1308 $cm^{-1}$ mode.

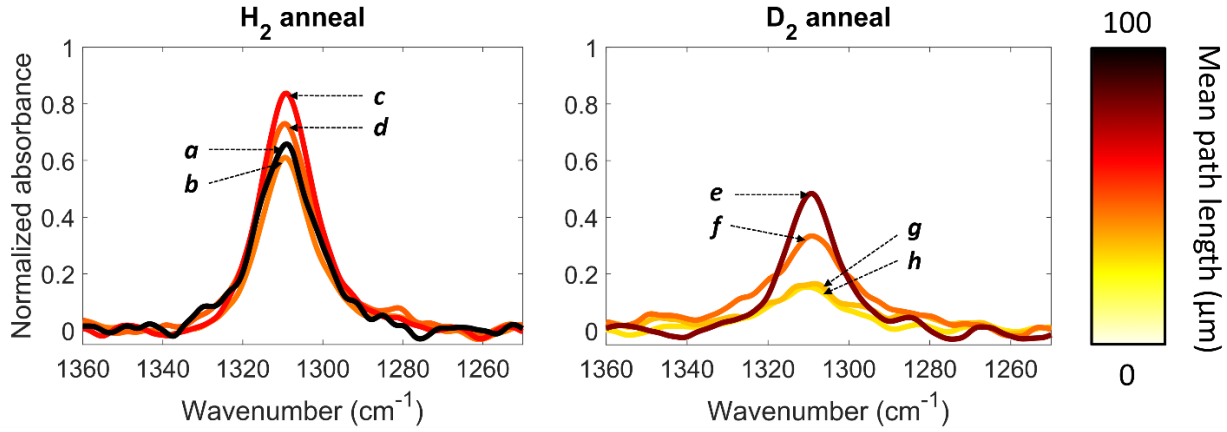


***Figure 6 –*** *Isolated 1308 $cm^{-1}$ bands from spectra taken in different sections of the dimpled $H_2$ and $D_2$ annealed samples. All spectra are normalized to their mean path length in cm and color weighted based on their path length. For the $H_2$ sample, there is a distribution in the 1308 cm-1 intensity, but no systematic variance with path length. For the D2 sample, the 1308 cm-1 is reduced relative to the H2 sample at all path lengths and systematically decreases with decreasing path length. This indicates a reduction in band intensity at sample volumes closer to the surface, consistent with H-D exchange. Sample thickness corresponding to each plotted spectrum: a – 100 μm, b – 45 μm, c – 62 μm, d – 49 μm, e - 81 μm, f – 47 μm, g – 35 μm, h – 30 μm.*

This result demonstrates that FTIR can have a higher sensitivity for $H^-$ detection than $^1H$ NMR, despite NMR's current status as the dominant form of analysis for this application. Across all the samples we analyzed via FTIR, there were no clearly resolvable $H^-$ peaks in any of the $^1H$ NMR spectra, even for those with the highest $H^-$ concentrations. Therefore, FTIR could prove to be a valuable technique for future studies of detecting hydride in oxide materials.

### The Structural State of Hydrogen

The current discussion on the structural state of hydrogen in reduced $SrTiO_3$ and other titanate perovskites reveals a complex landscape of possible defect states. Broad, negative shifted $^1H$ NMR features are unambiguously hydride-related and are thought to be a result of Knight shifts[3,4]. Misaki et al. (2019) proposed that Knight shifts result from H and Ti *3d* orbital hybridization in $BaTiO_3$, when $H^-$ resides off of the $O^{2-}$ lattice site[3]. However, Aleksis et al. (2022) conclude that Knight shifts in $CaH_2$-treated $BaTiO_3$ can be attributed to single hydride ions located directly on $O^{2-}$ sites[4]. $V_O$ was also found to contribute to the Knight shift, meaning that $^1H$ NMR feature positions may be equally indicative of oxygen deficiency in titanate perovskites. DFT results from Iwazaki et al. (2014) supported multiple possible $H^-$ configurations in $SrTiO_3$, where doubly occupied $V_O$ sites are stable[38]. Double occupations of this type could passivate reduced to $Ti^{3+}$ centers to $Ti^{4+}$, which would have a marked effect on sample color, conductivity and $^1H$ NMR shift. $H_2$ anneals can remove coloration and lower conductivity in reduced $SrTiO_3$ [10,12,34], possibly pointing to the stability of the doubly occupied $H^-$ state. Considering the present results in this context, the dominant state of hydride in $SrTiO_3$ is

likely a single $H^-$ at the $V_O$ site. One factor in this assignment is the initial intense coloration of the samples, which would seem to rule out full passivation of $Ti^{3+}$ to $Ti^{4+}$, via double occupation (although it should be acknowledged that this observation does not necessarily rule out the possibility of coexisting singly and doubly occupied $V_O$ sites). Nevertheless, the presence of only a single IR-active vibrational mode in close vicinity to the DFT-predicted Ti-H-Ti stretching frequency also implies that only one $H^-$ structural state is present.

**Explanation for the Vacuum and $H_2$ Annealing Behavior**

Despite confidence in assigning the 1308 $cm^{-1}$ feature to hydride, there remain some unusual spectroscopic behaviors from the vacuum and hydrogen annealed samples. First of these is the replacement of the 585 nm IVCT band by the 513 nm *d-d* transition band. The former appears to be intrinsically tied to structural hydride, but it was virtually eliminated when samples were subjected to either $H_2$ or vacuum heating, even when significant hydride signal remained. This change in the visible light spectrum could be due to a change in the localization of charge around $Ti^{3+}$ sites. IVCT absorptions imply a delocalization of the excess negative charge associated with Ti reduction. Meanwhile, a *d-d* transition implies the localization of charge to Ti, forming a long-lived, more isolated $Ti^{3+}$ state. This isolated $Ti^{3+}$ could be approximately equivalent to the polaron-like state explored by Eklöf-Österberg et al. (2020) and Aleksis et al. (2022) in $BaTiO_3$ [4,13].

Transitions between these states seem to be dependent on temperature, as this change occurs under both vacuum and a hydrogen atmosphere. The 513 nm band was observed in every sample that was treated at temperatures of 500 °C or below (see visible light spectra in Figures 4 and 5) and also coexists with the 585 nm IVCT band in sample SC-6006h (Figure 3). One possibility is that heating at temperatures high enough for diffusion processes, but too low for significant O or H loss could allow $H^-$ defect centers to become more spread out. Initial $CaH_2$ treatments likely lead to zones of many adjacent occupations by $H^-$. When the density of $H^-$ occupations is high, the excess Ti electrons can become delocalized, and IVCT may occur. This results in the 585 nm band (and perhaps contributes to the 2170 $cm^{-1}$ band as well). Once the crystals are heated, these $H^-$ occupancies can become more dispersed, and their associated $Ti^{3+}$ centers do as well. More advanced studies utilizing techniques that can target nanoscale distributions of H and lattice distortions would be necessary to confirm whether this explanation is valid.

The disappearance of the 2170 $cm^{-1}$ IVCT band also raises concerns. Normally, the disappearance of this feature would be associated with oxidation of a reduced $SrTiO_3$ crystal, as its presence is a hallmark of oxygen vacancies. However, virtually no oxygen is available under either of the treatment conditions. This is especially puzzling for the sample Vac3, which appears to have returned to the pristine $SrTiO_3$ state after progressive annealing under vacuum. One possible explanation for this is the progressive loss of Sr into the vapor phase. By coupling a Sr vacancy to a preexisting oxygen vacancy, charge balance can be achieved without the need for oxygen to reincorporate into $SrTiO_3$. The coupled Sr and O vacancies carry a net neutral charge as a Schottky defect, effectively passivating the $Ti^{3+}$ centers associated with the respective O vacancy or hydride and removing all IVCT and *d-d* bands. At the annealing temperatures tested, the vapor pressure of metallic Sr is below 1 mbar, but still high enough that a defect-level concentration of Sr could conceivably be removed from the bulk sample. However, for Sr to be removed as a vapor, it must be reduced from $Sr^{2+}$ to $Sr^0$ (metallic Sr). This reduction of $Sr^{2+}$ could be achieved through the simultaneous oxidation of $H^-$ to $H_2$ and $Ti^{3+}$ to $Ti^{4+}$. For samples under vacuum, as Sr is reduced, significant amounts of hydride are oxidized and lost as $H_2$. Under an atmosphere of $H_2$, this redox process may preferentially target $Ti^{3+}$ centers associated with $V_O$ for oxidation rather than $H^-$, as the partial pressure of $H_2$ is too high for hydrogen loss. This could explain how the 2170 $cm^{-1}$ band was weakened in sample H2-70024h while the 1308 $cm^{-1}$ band remained virtually unchanged. Nevertheless, it should be emphasized that further work utilizing techniques that can monitor real time Sr loss

(for example, continuous flow mass spectrometry methods analyzing the products released from the sample) would be necessary to confirm whether this truly is the mechanism at play.

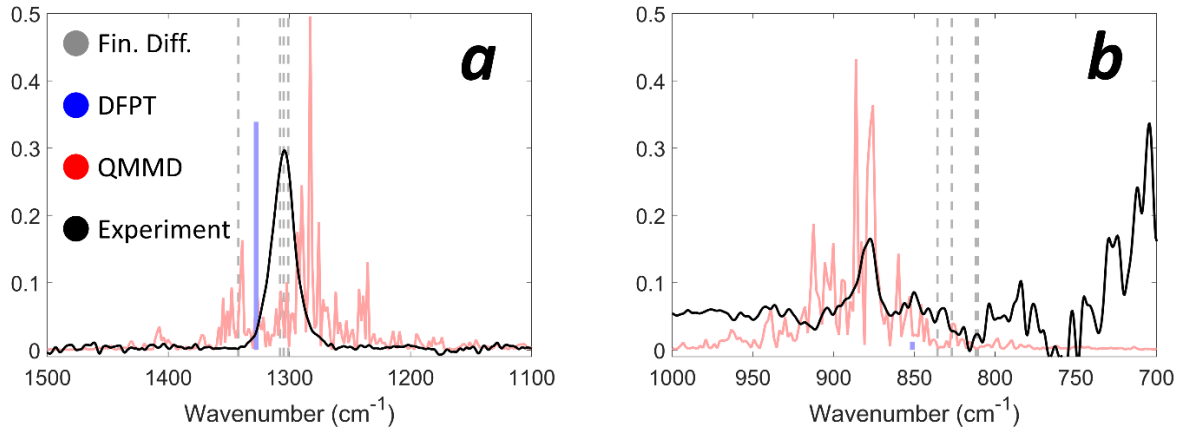


***Figure 7*** *– Comparison of the QM-MD calculated partial vDOS, 3x3x2 supercell DFPT calculated mode, finite difference calculated modes and the experimental data. (**a**) The stretching mode calculations are compared to the 1308 $cm^{-1}$ mode isolated from the infrared spectrum of SC-70048h. (**b**) Bending mode calculations are compared to a feature isolated from the same spectrum at 872 $cm^{-1}$. The DFT methods employed seem to be accurate enough to predict the position of both modes within a few 10s of $cm^{-1}$.*

**Accuracy of DFT Applied to Hydride**

DFT techniques have been applied extensively to making predictions about the infrared behavior of hydrogen, although most discussions concern $OH^-$. What has not been explored as extensively is the ability of these methods to make predictions about $H^-$ related modes. Assuming the assignment of the 1308 $cm^{-1}$ mode to the Ti-H-Ti vibration is correct, the PBE functional can predict hydride's vibrational behavior in $SrTiO_3$ with good accuracy. The DFPT result differs from experiment by only 19 $cm^{-1}$, while the QMMD partial vDOS contains a peak at ~1282 $cm^{-1}$, a difference on the order of 20 - 30 $cm^{-1}$ (Figure 7). Despite the apparent accuracy of theory applied to $SrTiO_3$, assessment of just one material is not enough to make claims about DFT's overall efficacy when applied to hydride-containing oxide systems. Eklöf-Österberg et al., 2020 were able to successfully observe Ti-H-Ti stretching and bending modes in hydride $BaTiO_3$ powders via inelastic neutron scattering. Subsequently, their finite differences calculations showed a tendency for the PBE functional to underestimate mode energies on the order of 15 to 60 $cm^{-1}$, while HSE techniques had greater accuracy[13]. Thus, unsurprisingly, functional choice plays a key role in prediction accuracy. The choice of pseudopotential for each ion is also likely to have a large effect on these errors. This could be a factor in the variability of errors in hydride mode positions seen across materials with different cations and bonding geometries. Janotti et al., 2007 predicted the positions of hydride-related modes for MgO and ZnO[39]. In multiple studies, hydride containing MgO has produced IR-active modes at 1024, 1032, and 1053 $cm^{-1}$, differing from Janotti et al. 2007's predicted position (950 $cm^{-1}$) by 74 to 103 $cm^{-1}$ [16,39,40]. Koch et al., 2012 observed $H^-$ associated modes in ZnO centered at 742 and 792 $cm^{-1}$ via photoconductivity measurements, for a discrepancy of 22 to 32 $cm^{-1}$ from Janotti et al., 2007 and 19 to 69 $cm^{-1}$ from a later study[41,42]. In Be-doped natural $Al_2O_3$, Jollands and Balan 2022 predicted Be-H groups would have a vibrational mode of 2602 $cm^{-1}$, while they observed Be-associated modes at 2491 $cm^{-1}$ and 2523 $cm^{-1}$ giving a potential error range of 111 to 79 $cm^{-1}$ [18]. Collectively, this series of computational and experimental comparisons suggest that commonly employed DFT methods show promise for predicting the positions of hydride modes in oxides, albeit with variable and modest errors.

The available DFT-experimental comparisons for $H^-$ in oxides remains limited to just a handful examples. For other materials where $H^-$ is predicted as stable, like rutile-type $TiO_2$ [43] and $SnO_2$ [44], $H^-$-associated vibrational modes have yet to be experimentally identified. $H^-$ modes have also been observed in some materials that

have not yet been investigated via DFT, namely CaO and SrO[16], leaving open the possibility for future studies in this vein.

**Expansion of Synthesis Parameters – $SrTiO_3$ and Beyond**

The present work conclusively demonstrates that hydride may be incorporated into $SrTiO_3$ crystals through reaction with $CaH_2$ at temperature conditions up to at least 800 °C. Prior studies placed the upper limit of these reactions at ~600° C, likely under the assumption that $CaH_2$ decomposes at higher temperatures. However, in a closed system where the evolved $H_2$ gas from $CaH_2$ cannot escape (like the sealed tubes in the present work), $CaH_2$ will not completely decompose, but rather equilibrate to some pressure of $H_2$. At 800° C, this pressure is on the order of approximately $2.3\times10^4$ Pa [45], corresponding to the decomposition of only about 2 mg of $CaH_2$ in the sample tubes used. Studies on hydride doping of other oxides have already demonstrated this in reactions involving other hydride rea.gents, like the reaction of hydroxyapatite ceramics with $TiH_2$ [46]. The preferable kinetics afforded by higher temperature reactions with $CaH_2$ and other hydrides could present new pathways for introducing hydride and oxygen vacancies into a range of oxide materials.

## Conclusions

Aided by QM results, strong evidence is provided for identifying hydride speciation in $SrTiO_3$ perovskite crystals through infrared spectroscopy. DFT predictions proved crucial in the identification of the hydride mode at 1308 $cm^{-1}$, as the feature both overlaps closely with a native $SrTiO_3$ feature at 1326 $cm^{-1}$ and occurs in a highly absorbing region of reduced $SrTiO_3$'s infrared spectrum. The former of these factors could make low concentrations of hydride easy to overlook without the prior knowledge provided by DFT. Additionally, infrared spectroscopy can be significantly more sensitive to hydride than $^1$H NMR, which is the technique most often employed in searching for hydride in oxide materials. Therefore, FTIR may prove valuable in the future studies of oxyhydrides, especially in materials where hydride is present in nonstoichiometric concentrations.

The use of FTIR could also expand the study of oxyhydrides to additional contexts where the more frequently used analytical methods of neutron scattering and thermally polarized-$^1$H NMR are impractical. For example, FTIR is suited for making *in situ* measurements in high pressure cells and analyzing small sample volumes. This means FTIR is a potentially key analytical tool for future studies of the interior of earth and other planetary bodies, where perovskite materials are abundant, and the possibility of hydride has been given limited consideration.

In addition to the identification of hydride via FTIR, a number of unusual spectroscopic behaviors were also observed that seem to associate with incorporation of hydride and its structural evolution in the $SrTiO_3$ lattice. There is implication that the electronic structure of $SrTiO_3$ could possibly be fine-tuned via manipulation of structural hydride, and future studies of the interplay between hydride and the electronic features at 513 nm, 585 nm, and 2170 $cm^{-1}$ could prove fruitful.

**Author contributions**

Conceptualization: W.R.P; Formal analysis: W.R.P.; Funding acquisition: W.A.G., G.R.R.; Investigation: W.R.P., S.J.H.; Methodology: W.R.P.; Supervision: W.A.G., G.R.R.; Writing – original draft: W.R.P.; Writing – review & editing: W.R.P., S.J.H, W.A.G., G.R.R.

**Conflicts of interest**

There are no conflicts to declare.

**Data availability**

The data supporting this article have been included as part of the Supplementary Information.

**Acknowledgements**

The authors thank Dr. Channing Ahn and Dr. Cullen Quine for providing access to facilities necessary for sample preparation. W.A.G. thanks NSF (CBET 2311117) for support. G.R.R. thanks NSF (EAR-2149559).

**References**

1 T. Sakaguchi, Y. Kobayashi, T. Yajima, M. Ohkura, C. Tassel, F. Takeiri, S. Mitsuoka, H. Ohkubo, T. Yamamoto, J. eun Kim, N. Tsuji, A. Fujihara, Y. Matsushita, J. Hester, M. Avdeev, K. Ohoyama and H. Kageyama, *Inorg. Chem.*, 2012, **51**, 11371–11376.

2 Y. Kobayashi, O. J. Hernandez, T. Sakaguchi, T. Yajima, T. Roisnel, Y. Tsujimoto, M. Morita, Y. Noda, Y. Mogami, A. Kitada, M. Ohkura, S. Hosokawa, Z. Li, K. Hayashi, Y. Kusano, J. eun Kim, N. Tsuji, A. Fujiwara, Y. Matsushita, K. Yoshimura, K. Takegoshi, M. Inoue, M. Takano and H. Kageyama, *Nature Mater*, 2012, **11**, 507–511.

3 T. Misaki, I. Oikawa and H. Takamura, *Chem. Mater.*, 2019, **31**, 7178–7185.

4 R. Aleksis, R. Nedumkandathil, W. Papawassiliou, J. P. Carvalho, A. Jaworski, U. Häussermann and A. J. Pell, *Phys. Chem. Chem. Phys.*, 2022, **24**, 28164–28173.

5 J. B. Varley, A. Janotti and C. G. Van de Walle, *Phys. Rev. B*, 2014, **89**, 075202.

6 T. Gao, L. Nian, L. Jin, H. Sun, T. Zhang, J. Yang, Z. Gu, L. Peng and Y. Nie, *Adv Elect Materials*, 2023, **9**, 2300068.

7 T. Yajima, F. Takeiri, K. Aidzu, H. Akamatsu, K. Fujita, W. Yoshimune, M. Ohkura, S. Lei, V. Gopalan, K. Tanaka, C. M. Brown, M. A. Green, T. Yamamoto, Y. Kobayashi and H. Kageyama, *Nature Chem*, 2015, **7**, 1017–1023.

8 R. Nedumkandathil, A. Jaworski, J. Grins, D. Bernin, M. Karlsson, C. Eklöf-Österberg, A. Neagu, C.-W. Tai, A. J. Pell and U. Häussermann, *ACS Omega*, 2018, **3**, 11426–11438.

9 H. Guo, A. Jaworski, Z. Ma, A. Slabon, Z. Bacsik, R. Nedumkandathil and U. Häussermann, *RSC Adv.*, 2020, **10**, 35356–35365.

10 W. Gong, H. Yun, Y. B. Ning, J. E. Greedan, W. R. Datars and C. V. Stager, *Journal of Solid State Chemistry*, 1991, **90**, 320–330.

11 J. Hanzig, B. Abendroth, F. Hanzig, H. Stöcker, R. Strohmeyer, D. C. Meyer, S. Lindner, M. Grobosch, M. Knupfer, C. Himcinschi, U. Mühle and F. Munnik, *Journal of Applied Physics*, 2011, **110**, 064107.

12 S. Mochizuki, F. Fujishiro, K. Ishiwata and K. Shibata, *Physica B: Condensed Matter*, 2006, **376–377**, 816–819.

13 C. Eklöf-Österberg, L. Mazzei, E. J. Granhed, G. Wahnström, R. Nedumkandathil, U. Häussermann, A. Jaworski, A. J. Pell, S. F. Parker, N. H. Jalarvo, L. Börjesson and M. Karlsson, *J. Mater. Chem. A*, 2020, **8**, 6360–6371.

14 F. Takeiri, K. Aidzu, T. Yajima, T. Matsui, T. Yamamoto, Y. Kobayashi, J. Hester and H. Kageyama, *Inorg. Chem.*, 2017, **56**, 13035–13040.

15 Alexander Mutschke, Thomas Wylezich, Clemens Ritter, Antti J. Karttunen, and Nathalie Kunkel, *European Journal of Inorganic Chemistry*, 2019, **48**, 5073–5076.

16 R. González, Y. Chen and M. Mostoller, *Phys. Rev. B*, 1981, **24**, 6862–6869.

17 A. Mutschke, G. M. Bernard, M. Bertmer, A. J. Karttunen, C. Ritter, V. K. Michaelis and N. Kunkel, *Angew Chem Int Ed*, 2021, **60**, 5683–5687.

18 M. C. Jollands and E. Balan, *MinMag*, 2022, **86**, 758–766.

19 T. Wylezich, R. Valois, M. Suta, A. Mutschke, C. Ritter, A. Meijerink, A. J. Karttunen and N. Kunkel, *Chemistry A European J*, 2020, **26**, 11742–11750.

20 T. Yajima, K. Takahashi, H. Nakajima, T. Honda, K. Ikeda, T. Otomo and Z. Hiroi, *Inorg. Chem.*, 2022, **61**, 2010–2016.

21 Y. Goto, C. Tassel, Y. Noda, O. Hernandez, C. J. Pickard, M. A. Green, H. Sakaebe, N. Taguchi, Y. Uchimoto, Y. Kobayashi and H. Kageyama, *Inorg. Chem.*, 2017, **56**, 4840–4845.
22 H.-K. Mao, Q. Hu, L. Yang, J. Liu, D. Y. Kim, Y. Meng, L. Zhang, V. B. Prakapenka, W. Yang and W. L. Mao, *National Science Review*, 2017, **4**, 870–878.
23 J. P. Perdew, K. Burke and M. Ernzerhof, *Phys. Rev. Lett.*, 1996, **77**, 3865–3868.
24 J. P. Perdew, K. Burke and M. Ernzerhof, *Phys. Rev. Lett.*, 1997, **78**, 1396–1396.
25 G. Kresse and J. Furthmüller, *Computational Materials Science*, 1996, **6**, 15–50.
26 G. Kresse and J. Furthmüller, *Phys. Rev. B*, 1996, **54**, 11169–11186.
27 G. Kresse and J. Hafner, *Phys. Rev. B*, 1993, **47**, 558–561.
28 G. Kresse and D. Joubert, *Phys. Rev. B*, 1999, **59**, 1758–1775.
29 P. E. Blöchl, O. Jepsen and O. K. Andersen, *Phys. Rev. B*, 1994, **49**, 16223–16233.
30 D. Karhánek, dakarhanek/VASP-infrared-intensities (version v1.0) Zenodo 2020.
31 S.-T. Lin, M. Blanco and W. A. Goddard, *The Journal of Chemical Physics*, 2003, **119**, 11792–11805.
32 S.-T. Lin, P. K. Maiti and W. A. Goddard, *J. Phys. Chem. B*, 2010, **114**, 8191–8198.
33 T. A. Pascal, S.-T. Lin and W. A. Goddard III, *Phys. Chem. Chem. Phys.*, 2011, **13**, 169–181.
34 B. Jalan, R. Engel-Herbert, T. E. Mates and S. Stemmer, *Applied Physics Letters*, 2008, **93**, 052907.
35 J. Eills, D. Budker, S. Cavagnero, E. Y. Chekmenev, S. J. Elliott, S. Jannin, A. Lesage, J. Matysik, T. Meersmann, T. Prisner, J. A. Reimer, H. Yang and I. V. Koptyug, *Chem. Rev.*, 2023, **123**, 1417–1551.
36 P. D. Ihinger and E. Stolper, *Earth and Planetary Science Letters*, 1986, **78**, 67–79.
37 P. F. Moulton, J. G. Cederberg, K. T. Stevens, G. Foundos, M. Koselja and J. Preclikova, *Opt. Mater. Express*, 2019, **9**, 2216.
38 Y. Iwazaki, Y. Gohda and S. Tsuneyuki, *APL MATERIALS*, 2014, **2**, 012103.
39 A. Janotti and C. G. Van de Walle, *Nature Mater*, 2007, **6**, 44–47.
40 R. González, I. Vergara, D. Cáceres and Y. Chen, *Phys. Rev. B*, 2002, **65**, 224108.
41 S. G. Koch, E. V. Lavrov and J. Weber, *Phys. Rev. Lett.*, 2012, **108**, 165501.
42 M.-H. Du and D. J. Singh, *Phys. Rev. B*, 2009, **79**, 205201.
43 W. R. Palfey, G. R. Rossman and W. A. Goddard, *J. Phys. Chem. Lett.*, 2021, **12**, 10175–10181.
44 A. K. Singh, A. Janotti, M. Scheffler and C. G. Van de Walle, *Phys. Rev. Lett.*, 2008, **101**, 055502.
45 E. P. Kilb, *Literature Survey on Calcium Hydride*, General Electric, Atomic Products Division, 1959.
46 K. Hayashi and H. Hosono, *Phys. Chem. Chem. Phys.*, 2016, **18**, 8186–8195.